IOP Conf. Series: Journal of Physics: Conf. Series **1001** (2018) 012011 doi:10.1088/1742-6596/1001/1/012011

# Manipulation of near-wall turbulence by surface slip and permeability

**G. Gómez-de-Segura, C. T. Fairhall, M. MacDonald, D. Chung and R. García-Mayoral**

Department of Engineering, University of Cambridge, Trumpington St, Cambridge CB2 1PZ, UK

E-mail: r.gmayoral@eng.cam.ac.uk

**Abstract.** We study the effect on near-wall turbulence of tangential slip and wall-normal transpiration, typically produced by textured surfaces and other surface manipulations. For this, we conduct direct numerical simulations (DNSs) with different virtual origins for the different velocity components. The different origins result in a relative wall-normal displacement of the near-wall, quasi-streamwise vortices with respect to the mean flow, which in turn produces a change in drag. The objective of this work is to extend the existing understanding on how these virtual origins affect the flow. In the literature, the virtual origins for the tangential velocities are typically characterised by slip boundary conditions, while the wall-normal velocity is assumed to be zero at the boundary plane. Here we explore different techniques to define and implement the three virtual origins, with special emphasis on the wall-normal one. We investigate impedance conditions relating the wall-normal velocity to the pressure, and linear relations between the velocity components and their wall-normal gradients, as is typically done to impose slip conditions. These models are first tested to represent a smooth wall below the boundary plane, with all virtual origins equal, and later for different tangential and wall-normal origins. Our results confirm that the change in drag is determined by the offset between the origins perceived by mean flow and the quasi-streamwise vortices or, more generally, the near-wall turbulent cycle. The origin for the latter, however, is not set by the spanwise virtual origin alone, as previously proposed, but by a combination of the spanwise and wall-normal origins, and mainly determined by the shallowest of the two. These observations allow us to extend the existing expression to predict the change in drag, accounting for the wall-normal effect when the transpiration is not negligible.

## 1. Introduction

The use of complex surfaces to reduce turbulent skin friction is an area of active scientific and practical interest. Some of the most popular techniques include riblets [1], superhydrophobic surfaces [2] or permeable substrates [3, 4]. It is generally accepted that the drag reduction produced by these surfaces is due to the cross flow being more severely hindered than the streamwise mean flow. Luchini *et al.* [5, 6] and Jiménez [7] provided an expression to estimate quantitatively the change in drag produced by these surfaces. If the surface texture is small compared to the near-wall turbulent structures, the overlying flow perceives the texture as a uniform surface, inducing a homogeneous shear in the streamwise and spanwise directions. However, the virtual wall from which the streamwise and spanwise velocities originate can differ. The effect of the texture can then be reduced to a reference plane with non-zero velocities,

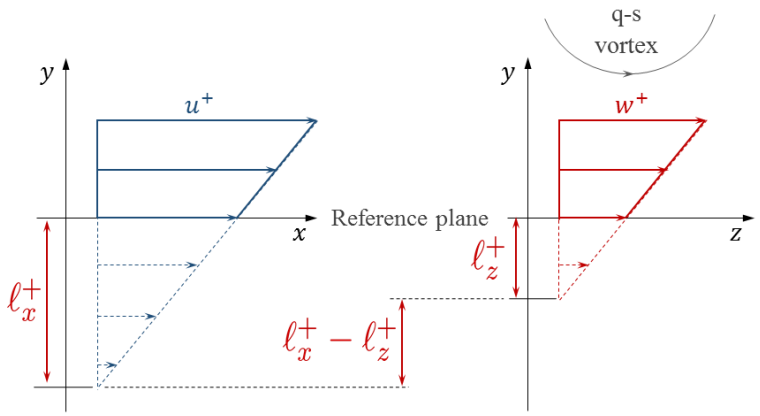


Figure 1: Sketch of streamwise and spanwise slip lengths. The term 'q-s vortex' refers to quasi-streamwise vortex.

contrary to conventional smooth walls, where all velocity components are zero at the surface. This reference plane is generally taken at the top plane of the surface geometry, such as at the riblet tips or at the plane above the gas pockets for superhydrophobic surfaces. The effect of the texture is typically modelled by slip boundary conditions at this reference plane $y = 0$, $u|_{slip} = \ell_x \, \partial u/\partial y|_{y=0}$ and $w|_{slip} = \ell_z \, \partial u/\partial y|_{y=0}$, where $\ell_x$ and $\ell_z$ are the streamwise and spanwise slip lengths, or alternatively, virtual origins. The slip lengths, $\ell_x$ and $\ell_z$, are defined as the depth below the reference plane where the streamwise and spanwise velocities induced by the overlying shear become zero when extrapolated. These concepts are portrayed in Figure 1. In the superhydrophobic community the term 'slip length' is used to denote virtual origins, while in the riblet community the term 'protrusion height' is used instead. Note that throughout this paper we will consider $x, y, z$ for the streamwise, wall-normal and spanwise coordinates and $u, v, w$ for the velocity components in $x$, $y$ and $z$ directions.

The classical theory of wall turbulence suggests that, sufficiently far away from the wall, the only appreciable effect of surface manipulations is to modify the intercept of the logarithmic velocity profile, while the Kármán constant remains unaltered [8]. Therefore, the change in drag with respect to the smooth wall is directly related to the change of the intercept of the velocity profile, $\Delta U^+$, where the superscript '+' denotes viscous units. An upward shift of the logarithmic region, $\Delta U^+ > 0$, translates into a decrease in drag, and vice-versa. Following the theory of Luchini *et al.* [5] and Jiménez [7], for sufficiently small surface textures the change in drag or $\Delta U^+$ is given by the difference between the streamwise and the spanwise slip lengths scaled in viscous units,

$$\Delta D \propto \Delta U^+ = \mu_0 \left( \ell_x^+ - \ell_z^+ \right), \tag{1}$$

where $\mu_0$ is a universal constant, estimated as $\mu_0 \approx 0.785$ in [9] and $\mu_0 \approx 0.66$ in [7]. From a physical point of view, Eq. (1) indicates that the change in drag is due to a relative $y$-displacement of the quasi-streamwise vortices with respect to the mean flow. If the overlying spanwise flow, which is essentially induced by quasi-streamwise vortices, is hindered more than the mean streamwise flow, the virtual origin seen by quasi-streamwise vortices is above that seen by the mean flow, i.e. $\ell_z^+ < \ell_x^+$. Compared to a smooth wall, the vortices are 'pushed' further away from the streamwise virtual origin, even if they approach the reference plane. As a result, the local momentum flux close to the streamwise virtual origin decreases, thereby reducing the friction drag. Conversely, if $\ell_x^+ < \ell_z^+$, the vortices move closer to the origin of the mean flow, and friction drag increases.

This linear theory is only valid as long as the texture length scales are small compared to the

characteristic length scales of near wall turbulence. In the vicinity of the wall, the smallest typical length scale is the characteristic diameter of quasi-streamwise vortices, which is approximately 15 wall units [7]. As the texture size increases, the turbulent structures begin to perceive the surface texture. They no longer perceive the presence of the texture as a homogeneous slip, and the linear slip-length model in Eq. (1) breaks down [10, 11].

However, Fukagata *et al.* [12] and Busse & Sandham [13] observed that the linear dependence in Eq. (1) breaks down for spanwise slip lengths smaller than expected, of the order of $\sim 1$ wall unit. Beyond $\ell_z^+ \approx 1$, the spanwise slip length saturates. This saturation effect can be observed in Figure 2a, where the change in drag in terms of $\Delta U^+$ obtained by Busse & Sandham [13] for a wide range of $\ell_x^+$ and $\ell_z^+$ is portrayed. Analysing their results, the change in drag can still be represented by an expression similar to Eq. (1), if an effective spanwise slip length, $\ell_{z,eff}^+$, is used instead of $\ell_z^+$. The shift in the velocity profile is then $\Delta U^+ \propto \left(\ell_x^+ - \ell_{z,eff}^+\right)$, where $\ell_{z,eff}^+$ is empirically found from their data to be

$$\ell_{z,eff}^+ = \frac{\ell_z^+}{1 + \ell_z^+/4}. \tag{2}$$

The two-dimensional parametric space can then be fitted into a single curve, as shown in Figure 2b. This results would be consistent with $\mu_0 \approx 1$ in Eq.(1). The data shows that isotropic textures with equal streamwise and spanwise slip lengths can also reduce drag, provided that the slip they induce is large enough, as the adverse effect of the spanwise slip saturates for $\ell_z^+ \gtrsim 1$. This is in agreement with the DNS results of Min & Kim [14], who studied the effect of streamwise and spanwise slip lengths independently as well as combined.

In this work, we will study the effect of introducing virtual origins for the tangential velocities, $u$ and $w$, and also for the wall-normal velocity, $v$. Although imposing a virtual origin for $u$ and $w$ in terms of slip lengths is very intuitive, defining a virtual origin for $v$ is not as simple, and the origin of $v$ has never been included in this framework. However, in the literature the effect of wall-normal velocity has been investigated separately [15], showing that turbulence is highly sensitive to transpiration, and it is, for instance, responsible for the eventual degradation of performance for drag-reducing technologies such as riblets [1]. The objective of this project is to study the effect of imposing different virtual origins for the three velocity components independently. In this paper, we conduct preliminary work with that aim, restricting ourselves to cases where all three virtual origins are the same, or cases where the origins for the tangential velocities are the same and that for the wall-normal velocity is zero. The paper is organised as follows. Firstly, the saturation of the spanwise slip length is discussed in Section 2. The numerical method, together with the models for defining virtual origins is presented in Section 3. Results are then presented in Section 4, followed by a discussion in Section 5. Finally, conclusions are summarised in Section 6.

## 2. Saturation of spanwise slip

As mentioned above, when the spanwise slip length increases beyond $\ell_z^+ \gtrsim 1$, its effect on the overlying flow saturates [13]. Consequently, equal slip lengths, $\ell_x^+ = \ell_z^+$, also lead to a decrease of drag, contrary to what the linear theory of slip lengths in Eq. (1) predicts. Note that both the simulations of [13] and the linear theory of slip lengths [5, 7] assume zero wall-normal velocity fluctuations at the reference plane. However, real surfaces that produce non-zero slips, such as riblets [1], porous substrates [16] or superhydrophobic surfaces [17], induce additionally a non-zero wall-normal velocity at the reference plane. The absence of transpiration in slip-only simulations leads to the saturation of the spanwise slip observed in Figure 2.

According to [5], the change in drag is due to a relative displacement of the streamwise mean flow and the quasi-streamwise vortices, but these vortices induce both spanwise and wall-normal

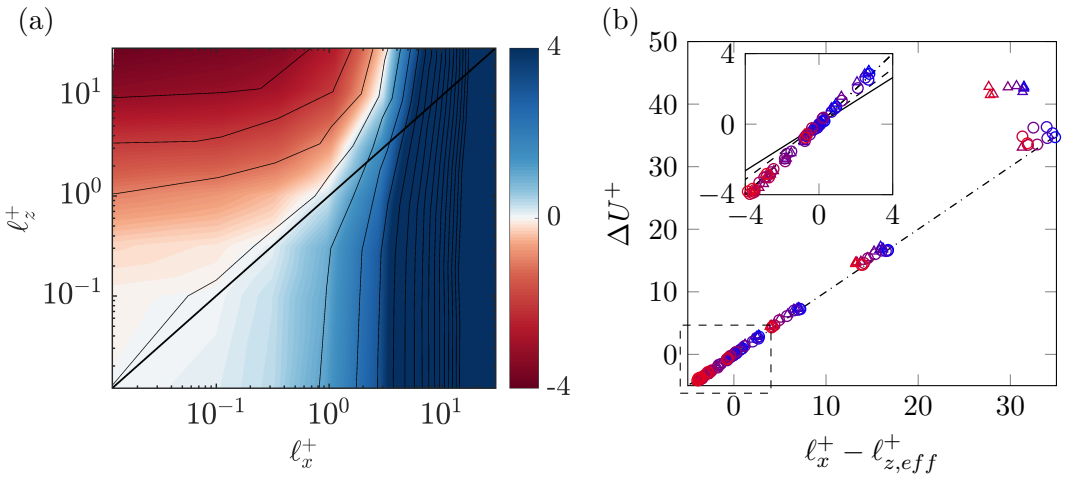


Figure 2: (a) Map of $\Delta U^+$ for different slip lengths, $\ell_x^+$ and $\ell_z^+$ from Busse & Sandham [13] for $Re_\tau = 180$. The black solid line corresponds to $\ell_x^+ = \ell_z^+$. (b) $\Delta U^+$ as a function of $\ell_x^+ - \ell_{z,eff}^+$, where $\ell_{z,eff}^+ = \ell_z^+/(1+\ell_z^+/4)$, using the same data as in (a). Triangles correspond to simulations at $Re_\tau = 180$ and circles at $Re_\tau = 360$. From blue to red the spanwise slip increases. The dash-dotted line represents Eq. (1) with the slope $\mu_0 = 1.0$. The inset shows a zoom for the small values, where the solid line represents Eq. (1) with the slope from [7], $\mu_0 = 0.66$; the dashed line that from [9, 6], $\mu_0 = 0.785$; and the dash-dotted line $\mu_0 = 1.0$.

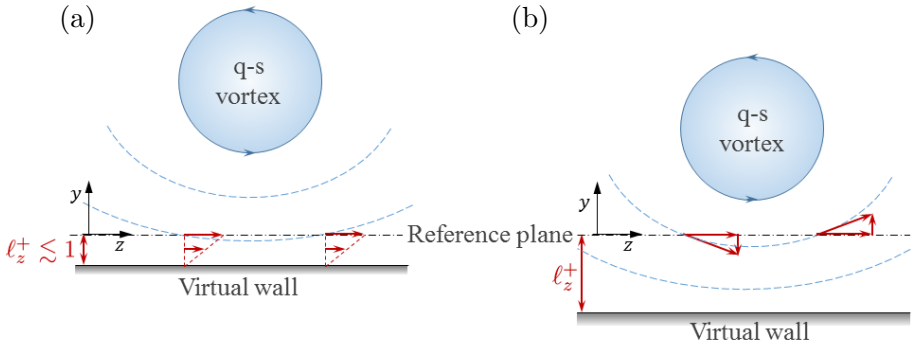


Figure 3: Schematic of the spanwise and wall-normal velocities induced by quasi-streamwise vortices at the reference plane for (a) virtual origins $\lesssim 1$ wall unit and (b) larger virtual origins.

velocities near the wall. Their distance to the wall would therefore not only be affected by the virtual origin for $w$, but also by the virtual origin for $v$. The sketch of quasi-streamwise vortices in Figure 3 helps to visualise this idea. For $\ell_z^+ \lesssim 1$, the wall-normal velocity induced by the vortices at the reference plane is small compared to the spanwise velocity (Figure 3a). Consequently, the effect of $v$ can be neglected and the virtual origin for the vortices is essentially that for the spanwise velocity. Therefore, for $\ell_z^+ \lesssim 1$ the change in drag is properly captured by the linear expression in Eq. 1, where the origin of quasi-streamwise vortices is set by that of the spanwise velocity alone, $\ell_z^+$.

On the other hand, if the reference plane is closer to the mean height of vortex cores, as in Figure 3b, the wall-normal velocity induced by the vortices at the reference plane is no longer negligible. When impeding $v$ at the reference plane, such as in the study by Busse & Sandham [13], the virtual origin that the vortices perceive is no longer set by $\ell_z^+$ alone, as the downward translation of the vortices is now restricted by $v$ being zero at the reference plane. For spanwise

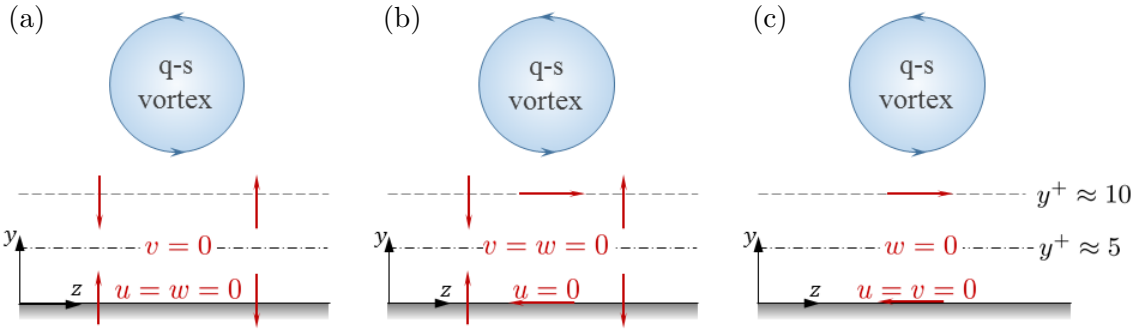


Figure 4: Schematics of the different control strategies studied by Choi *et al.* [18]. (a) *v-control*, (b) *v-w-control* and (c) *w-control*.

Table 1: Different control strategies studied by Choi *et al.* [18] and the equivalency with the displacement of virtual origins. The slip lengths are measured from the intermediate plane, i.e. the dash-dotted plane in Figure 4. Drag reduction (DR) is measured in terms of the change in the mean pressure gradient for a fixed mass flow rate.

| | *v-control* | *v-w-control* | *w-control* |
|---|---|---|---|
| $\ell_x^+$ | 5 | 5 | 5 |
| $\ell_z^+$ | 5 | 0 | 0 |
| $\ell_y^+$ | 0 | 0 | 5 |
| $DR$ | 25% | 30% | 30% |

slip lengths of a few wall units, for which the saturation has already been reached, a further increase of $\ell_z^+$ has little or no effect on the origin of the overlying turbulence, since the wall-normal velocity is zero at the reference plane and the quasi-streamwise vortices cannot approach it any further. For the vortices to move closer to the reference plane, the wall-normal velocity would also need to perceive a non-zero virtual origin, i.e. some form of transpiration would need to exist at the reference plane. In this paper, in addition to the streamwise and spanwise virtual origins traditionally defined, we will also include a virtual origin for the wall-normal velocity.

In retrospect, the opposition control studies of Choi *et al.* [18] can be interpreted as an alternative method of imposing different virtual origins for the different velocity components but, in contrast with [13, 7, 5, 6], including a non-zero virtual origin for $v$. This would suggest that some active control techniques are based on the same drag-reduction mechanism as passive controls. Choi *et al.* explored several active control strategies for the wall-normal and spanwise velocities, including opposition control of the wall-normal velocity alone (*v-control*), control of the spanwise velocity alone (*w-control*), and combined control of $v$ and $w$ (*v-w-control*). In each case, the velocity components imposed at the wall were opposite to those measured at $y^+ \approx 10$. The authors concluded that the reduction of skin friction in the three cases was a result to the outward shift of the origin of turbulence with respect to the mean flow. These simulations can be interpreted as imposing different origins for the different velocities, since imposing at $y^+ = 0$ a velocity equal and opposite to that at $y^+ = 10$ is roughly equivalent to imposing a zero velocity at $y^+ \approx 5$. Schematics for the three cases considered are shown in Figure 4. The drag reduction achieved, together with the equivalent virtual origins, taking as reference plane that at $y^+ = 5$, can be found in Table 1. Note that these values only allow for qualitative comparison, since the

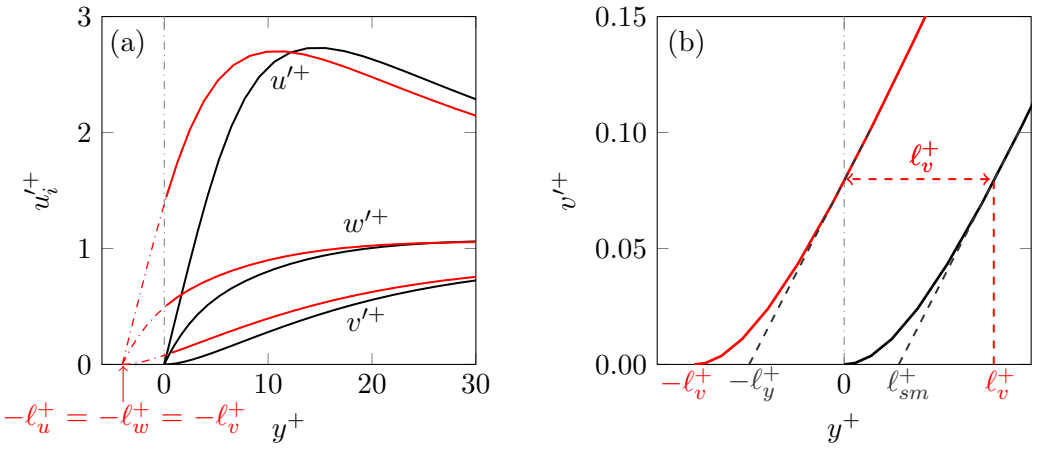


Figure 5: Schematics showing (a) the definition of the virtual origins $\ell_u^+$, $\ell_w^+$ and $\ell_v^+$ as the shift of the rms velocity fluctuations with respect to a smooth channel; (b) the difference between $\ell_v^+$ and $\ell_y^+$. Black, smooth channel; red, virtual origins equal and below the reference plane.

above analogy only produces a rough estimate of the effective virtual origins. The *v-control* case would be analogous to setting virtual origins $\ell_x^+ = \ell_z^+ = 5$ and $\ell_y^+ \approx 0$. This case corresponds to one of the cases from Busse & Sandham [13] portrayed in Figure 2, and a similar drag reduction is obtained, which is well captured by the modified drag-reduction expression introduced in Section 1, $\Delta U^+ \propto \left(\ell_x^+ - \ell_{z,eff}^+\right)$. The *v-w-control* case would be analogous to virtual origins $\ell_x^+ = 5$ and $\ell_y^+ = \ell_z^+ \approx 0$, which is also one of the cases from [13] included in Figure 2. The last case, *w-control*, is equivalent to imposing a virtual origin for $u$ and $v$, but not for $w$, which has not been considered in the previous studies, and corresponds to $\ell_x^+ = \ell_y^+ = 5$ and $\ell_z^+ \approx 0$. The obtained drag reduction is practically equal to that of the *v-w-control* case. By comparing *w-control* to *v-control*, it may be inferred that the effect of the spanwise slip length, $\ell_z^+$, is more restrictive than that of the wall-normal component, $\ell_y^+$.

Before moving to the modelling of virtual origins, some terms need to be defined. In the literature, the concepts of slip lengths and virtual origins have been used interchangeably, but here we will distinguish them. Hereinafter we will denote $\ell_x^+$, $\ell_z^+$ and $\ell_y^+$ as the slip lengths in the streamwise, spanwise and wall-normal directions. These slip lengths relate the velocities with their wall-normal gradients,

$$u|_{slip} = \ell_x \left.\frac{\partial u}{\partial y}\right|_{y=0}, \quad w|_{slip} = \ell_z \left.\frac{\partial w}{\partial y}\right|_{y=0} \quad \text{and} \quad v|_{slip} = \ell_y \left.\frac{\partial v}{\partial y}\right|_{y=0}, \tag{3}$$

and can be used to set Robin boundary conditions. Note that for $y$, $\ell_y$ does not convey a slip effect. The slip lengths simply correspond to the $y$-locations where the velocity components become zero if linearly extrapolated from the reference plane.

The virtual origins of $u$, $w$ and $v$, on the other hand, will be denoted by $\ell_u^+$, $\ell_w^+$ and $\ell_v^+$, respectively. These are obtained from the shifts of the rms velocity fluctuations, $u'^+$, $w'^+$ and $v'^+$ in the wall-normal direction with respect to the smooth channel profiles, as illustrated in Figure 5a. For small slip lengths, we expect the tangential slip lengths, $\ell_x^+$ and $\ell_z^+$, to be essentially equal to the virtual origins, $\ell_u^+$ and $\ell_w^+$. The case of $v$, however, is slightly more delicate. Due to the parabolic nature of the $v'$ profile at the wall, the virtual origin of $v$, $\ell_v^+$, differs from the slip length $\ell_y^+$ even for small values. From Figure 5b, we can observe that $\ell_y^+$ and $\ell_v^+$ relate to each other by $\ell_y^+ = \ell_v^+ - \ell_{sm}^+$, where $\ell_{sm}^+$ is obtained from extrapolating the

slope of $v'^+$ at $y^+ = \ell_v^+$ for a smooth channel. Note that the value of $\ell_{sm}^+$ is a function of $\ell_v^+$, as it depends on the local slope at which the extrapolation of the curve is calculated. Equivalently, the origins of the mean flow, $\ell_U^+$, and that of the quasi-streamwise vortices, $\ell_{\omega_x}^+$, are defined as the wall-normal displacement of the mean flow and the streamwise vorticity $\omega_x'^+$ with respect to the smooth channel case. The streamwise vorticity $\omega_x'^+$ is mainly due to quasi-streamwise vortices. It therefore provides a good measure to identify the translation of these vortices [18], as it will be observed in the results.

## 3. Numerical setup

In this section, the numerical setup for the simulations is presented together with the models used to define the virtual origins. We conduct simulations of channel flows with off-wall boundary conditions to represent the virtual origins for the three velocity components.

The DNS code is adapted from that of García-Mayoral & Jiménez [1]. The incompressible Navier-Stokes equations are solved using a fractional step method combined with a three-step Runge-Kutta [19] in a doubly-periodic channel of height $2\delta$. The spatial discretisation is spectral in $x$ and $z$ using Fourier series, and the wall-normal direction is discretised using a second-order centred finite difference scheme. Simulations are conducted at constant pressure gradient, starting from a smooth wall flow at $Re_\tau \simeq 180$, which is the Reynolds number based on the half-height of the channel and the friction velocity $u_\tau$. The size of the computational domain is $2\pi \times \pi \times 2$ in the streamwise, spanwise and wall-normal directions, respectively, and simulations are performed for a grid of $128 \times 128 \times 153$ points, which corresponds to a resolution of $\Delta x^+ \approx 8$, $\Delta z^+ \approx 4$ and $\Delta y^+ \simeq 0.3 - 3$.

The virtual origins below the simulation boundary are modelled by means of off-wall conditions for the three velocities, which have previously been used to model the presence of smooth walls below the simulation boundary [20, 21, 22]. Although traditionally Robin boundary conditions have been used to impose the tangential virtual origins in terms of slip lengths [14, 13], the origin for the wall-normal velocity has not been introduced in that framework. Therefore, before being able to set the virtual origins for the three velocities independently, we explore different techniques to represent $\ell_v^+$. Two different techniques are investigated:

a) an impedance condition [15], relating $v$ at the simulation boundary to the pressure, which is obtained assuming that the flow between the virtual wall and the simulation boundary is dominantly viscous and governed by Stokes equations. The off-wall conditions for this technique are detailed in subsection 3.1.
b) Robin off-wall conditions, defined in Eq. (3), which linearly relate the velocity components with their wall-normal gradients.

To validate the above models, we will first consider cases with the same virtual origin for all the velocities, which we will denote by a simple $\ell^+$ for simplicity ($\ell_u^+ = \ell_v^+ = \ell_w^+ = \ell^+$). If the technique is successful at mimicking a virtual wall at $y^+ = -\ell^+$, flow for a smooth channel with an actual wall at the height of the virtual origin should be recovered. Compared to a smooth channel, the turbulence statistics should then be shifted by an amount equal to the virtual origin, as in Figure 5a.

### *3.1. Stokes model*

To derive the off-wall conditions with the Stokes model we will consider cases for which the virtual origins for all the components are at the same $y$-location, $y^+ = -\ell^+$. If we consider a small $\ell^+$, the advective terms in the region delimited by $y^+ = -\ell^+$ and $y^+ = 0$ would be negligible compared to the viscous terms. The flow can thus be modelled as a Stokes flow. To obtain the off-wall conditions at $y^+ = 0$ for the DNSs, we solve analytically the Stokes equation,

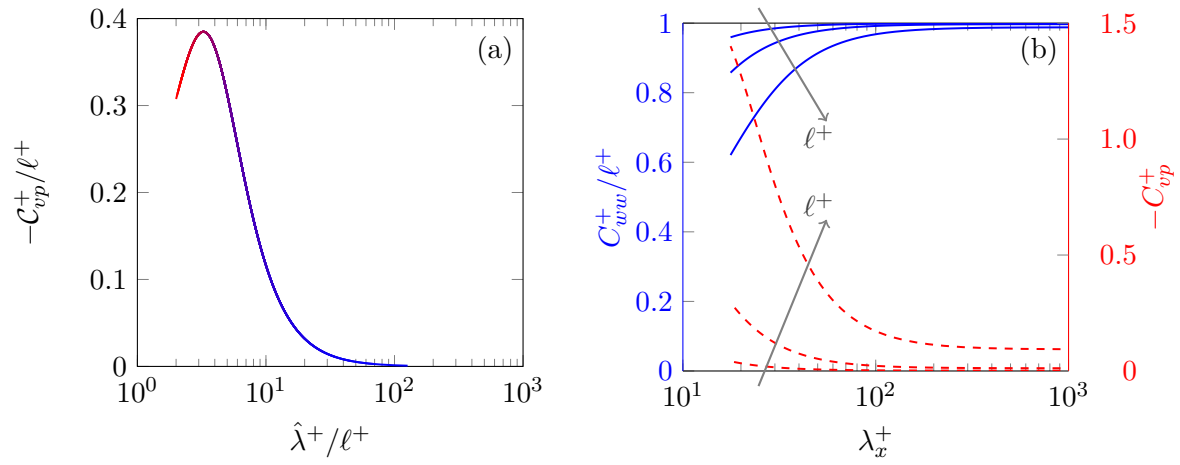


Figure 6: (a) Dimensionless transpiration coefficient $\mathcal{C}_{vp}/\ell^+$ as a function of the spherical wavelength $\hat{\lambda} = 2\pi/\sqrt{\alpha_x^2 + \alpha_z^2}$. (b) $\mathcal{C}_{vp}^+$, red dashed lines, and $\mathcal{C}_{ww}^+$, blue solid lines, for $\lambda_z^+ \approx 100$ as a function of $\lambda_x^+$ for three different virtual origins $\ell^+ = 1, 2$ and 4. Arrows indicate increasing $\ell^+$.

$-\nabla p + \nu\nabla^2\mathbf{u} = 0$, where $\mathbf{u} = (u, v, w)$ is the velocity vector in $(x, y, z)$ coordinates, and $\nu$ is the kinematic viscosity. We assume the density $\rho$ to be unity for convenience. The problem can be expanded using Fourier series in $x$ and $z$. The Stokes equation is then solved as a response to waves of tangential shear, $d\hat{u}/dy$ and $d\hat{w}/dy$, and pressure, $\hat{p}$, at $y^+ = 0$, where the hat indicates variables in Fourier space. At $y^+ = -\ell^+$, impermeability and no-slip conditions are applied. Considering these boundary conditions, the analytical solution of the problem provides the following relationships between the velocities and the pressure at $y^+ = 0$,

$$\hat{u}|_{y=0} = \mathcal{C}_{uu}\left.\frac{d\hat{u}}{dy}\right|_{y=0} + \mathcal{C}_{uw}\left.\frac{d\hat{w}}{dy}\right|_{y=0} + \mathcal{C}_{up}\hat{p}|_{y=0^+}\,, \tag{4a}$$

$$\hat{w}|_{y=0} = \mathcal{C}_{wu}\left.\frac{d\hat{u}}{dy}\right|_{y=0} + \mathcal{C}_{ww}\left.\frac{d\hat{w}}{dy}\right|_{y=0} + \mathcal{C}_{wp}\hat{p}|_{y=0^+}\,, \tag{4b}$$

$$\hat{v}|_{y=0} = \mathcal{C}_{vu}\left.\frac{d\hat{u}}{dy}\right|_{y=0} + \mathcal{C}_{vw}\left.\frac{d\hat{w}}{dy}\right|_{y=0} + \mathcal{C}_{vp}\hat{p}|_{y=0}\,. \tag{4c}$$

The constants $\mathcal{C}_{ij}$ depend on the virtual origin $\ell^+$, but also on the streamwise and spanwise wavelengths, $\lambda_x^+$ and $\lambda_z^+$. The corresponding expressions for the upper wall can be obtained by symmetry, and together they provide off-wall conditions for the flow within the channel. The dominant terms are those in the diagonal, i.e. $\mathcal{C}_{uu}$ and $\mathcal{C}_{ww}$ for $u$ and $w$, which would be equivalent to the slip lengths in the streamwise and spanwise directions, and $\mathcal{C}_{vp}$ for $v$, which would correspond to the impedance of [15].

To illustrate how the apparent permeability of the wall varies for different structures, the transpiration coefficient $\mathcal{C}_{vp}^+$ for different wavelengths is portrayed in Figure 6a. Note that the Stokes equation is isotropic in the $x$ and $z$ directions, meaning that $\mathcal{C}_{vp}^+$ follows a single curve when plotted against a spherical wavelength, $\hat{\lambda} = 2\pi/\sqrt{\alpha_x^2 + \alpha_z^2}$. Values in Figure 6a are scaled with the distance to the virtual wall, $\ell^+$. As observed in the figure, the reference plane is essentially impermeable to large structures, while the impermeability relaxes as the structures become smaller. Actual correlations of the pressure with the wall-normal velocity from direct observations in DNS are discussed in this volume by Sanmiguel Vila & Flores [23].

Table 2: Boundary conditions for the three velocity components for each case simulated. $Re_\tau$ is the Reynolds number measured at the virtual origin of the mean flow for each case, i.e. at $y^+ = -\ell_x^+$. The wavelength-dependent coefficients are obtained from solving the Stokes flow in $-\ell^+ < y^+ < 0$ (Figure 6)

.

| Case | $\hat{u}^+\vert_{y^+=0} =$ | $\hat{w}^+\vert_{y^+=0} =$ | $\hat{v}^+\vert_{y^+=0} =$ | $Re_\tau$ |
|---|---|---|---|---|
| $FP222$ | Eq. (4a)$= f(\alpha_x, \alpha_z)$ | Eq. (4b)$= f(\alpha_x, \alpha_z)$ | Eq. (4c)$= f(\alpha_x, \alpha_z)$ | 183 |
| $DIP222$ | $\mathcal{C}_{uu}^+(\alpha_x, \alpha_z)\frac{d\hat{u}}{dy}^+$ | $\mathcal{C}_{ww}^+(\alpha_x, \alpha_z)\frac{d\hat{w}}{dy}^+$ | $\mathcal{C}_{vp}^+(\alpha_x, \alpha_z)\hat{p}^+$ | 183 |
| $DHP222$ | $\ell_x^+\frac{d\hat{u}}{dy}^+$ | $\ell_z^+\frac{d\hat{w}}{dy}^+$ | $\mathcal{C}_{vp}^+(\alpha_x, \alpha_z)\hat{p}^+$ | 183 |
| $DHV222$ | $\ell_x^+\frac{d\hat{u}}{dy}^+$ | $\ell_z^+\frac{d\hat{w}}{dy}^+$ | $\ell_y^+\frac{d\hat{v}}{dy}^+$ | 184 |
| $DHV220$ | $\ell_x^+\frac{d\hat{u}}{dy}^+$ | $\ell_z^+\frac{d\hat{w}}{dy}^+$ | 0 | 183 |
| $FP444$ | Eq. (4a)$= f(\alpha_x, \alpha_z)$ | Eq. (4b)$= f(\alpha_x, \alpha_z)$ | Eq. (4c)$= f(\alpha_x, \alpha_z)$ | 181 |
| $DHP444$ | $\ell_x^+\frac{d\hat{u}}{dy}^+$ | $\ell_z^+\frac{d\hat{w}}{dy}^+$ | $\mathcal{C}_{vp}^+(\alpha_x, \alpha_z)\hat{p}^+$ | 185 |
| $DHV444$ | $\ell_x^+\frac{d\hat{u}}{dy}^+$ | $\ell_z^+\frac{d\hat{w}}{dy}^+$ | $\ell_y^+\frac{d\hat{v}}{dy}^+$ | 185 |
| $DHV440$ | $\ell_x^+\frac{d\hat{u}}{dy}^+$ | $\ell_z^+\frac{d\hat{w}}{dy}^+$ | 0 | 185 |

Additionally, in Figure 6b the dependence on the streamwise wavelength of the transpiration coefficient $\mathcal{C}_{vp}^+$ is compared to that of the slip coefficient, $\mathcal{C}_{ww}^+$, at $\lambda_z^+ = 100$ for a range of $\lambda_x^+$ and for different $\ell^+$. Structures of the size of streaks ($\lambda_x^+ \approx 1000$) and quasi-streamwise vortices ($\lambda_x^+ \approx 100$) are subject to essentially the same slip length as the mean, $\mathcal{C}_{ww}^+ = \ell^+$. Hence, the slip coefficient $\mathcal{C}_{ww}^+$ is practically homogeneous and it could be treated as such, as it will be shown in the next section. This, although not shown, is also the case for $\mathcal{C}_{uu}^+$. The transpiration $\mathcal{C}_{vp}^+$, however, is more sensitive to the wavelengths. Although $\mathcal{C}_{vp}^+$ is zero for very large $\hat{\lambda}^+$, its value increases as the wavelengths decrease. This can be observed for $\ell^+ = 4$ in Figure 6b, where the surface is already quite permeable for $\lambda_z^+ = 100$. Hence, while the dependence on the wavelength of $\mathcal{C}_{uu}^+$ and $\mathcal{C}_{ww}^+$ can be neglected, the wavelength-dependent nature of the transpiration coefficient $\mathcal{C}_{vp}^+$ needs to be accounted for.

### *3.2. Cases under study*

As previously mentioned, our first objective is to find appropriate slip and impedance boundary conditions at $y^+ = 0$ to mimic the effect of a wall at $y^+ = -\ell^+$. Once we have identified a suitable technique, we will extend the method to different virtual origins for the different velocities.

We explore the following alternatives:

a) First, we will consider the full conditions from Eq. (4), which are derived from solving the Stokes flow between $y^+ = -\ell^+$ and $y^+ = 0$. Three cases will be analysed, $\ell^+ = 1, 2$ and 4.

b) To later define different virtual origins for each velocity component, we eliminate the coupling between different components from Eq. (4), by retaining only the dominant terms for each component, i.e. the slip coefficients $\mathcal{C}_{uu}$ and $\mathcal{C}_{ww}$ for $u$ and $w$, and the transpiration coefficient $\mathcal{C}_{vp}$ for $v$. The idea is to later define these separately, as if due to different virtual origins.

c) In an attempt to define the virtual origins in a simpler manner, we will further simplify the boundary conditions from case b). Following previous studies on slip lengths [14, 13]

Table 3: Virtual origins for the velocities, $\ell_u^+$, $\ell_w^+$ and $\ell_v^+$, the mean flow, $\ell_U^+$, and quasi-streamwise-vortices, $\ell_{\omega_x}^+$, obtained from DNS for the different cases conducted. $\ell_{sm}^+$ corresponds is obtained from extrapolating the v-profile for a smooth channel, as defined in Figure 5b.

| | $FP222$ | $DIP222$ | $DHP222$ | $DHV222$ | $DHV220$ | $FP444$ | $DHP444$ | $DHV444$ | $DHV440$ |
|---|---|---|---|---|---|---|---|---|---|
| $\ell_u^+$ | 2.0 | 2.0 | 2.0 | 2.0 | 2.0 | 3.9 | 4.0 | 4.0 | 4.0 |
| $\ell_w^+$ | 2.1 | 1.7 | 1.7 | 2.0 | 2.0 | 5.7 | 4.0 | 3.0 | 3.1 |
| $\ell_v^+$ | 2.1 | 1.5 | 1.5 | 2.3 | 1.3 | 7.4 | 9.5 | 3.5 | 1.7 |
| $\ell_{sm}^+$ | – | – | – | 0.8 | 0.0 | – | – | 1.5 | 0.0 |
| $\ell_{mean}^+$ | 2.0 | 2.0 | 2.0 | 2.0 | 2.0 | 3.7 | 3.5 | 3.9 | 4.0 |
| $\ell_{\omega_x}^+$ | 2.1 | 1.5 | 1.5 | 2.0 | 1.3 | – | – | 3.0 | 1.7 |

and the discussion at the end of subsection 3.1 on wavelength dependence, we will impose homogeneous tangential slip lengths, $\ell_x^+$ and $\ell_z^+$, to model the virtual origins of $u$ and $w$, while keeping a wavelength-dependent transpiration, $\mathcal{C}_{vp}^+$, as before.

d) Alternatively, instead of conditions derived from Eq. (4), we implement Robin conditions as defined in Eq. 3, even for the wall-normal velocity. In a first approach to introducing different virtual origins for the different velocities, we will study cases with $\ell_x^+ = \ell_z^+ = 1, 2$ and 4 and $\ell_y^+ = 0$, as in [13], and compare them with the simulations $\ell_x^+ = \ell_z^+ = \ell_y^+ = 1, 2$ and 4.

The different simulations and their numerical parameters are summarised in Table 2. Each case is labelled with 2 or 3 letters followed by 3 numbers. The letters refer to the equations used as boundary conditions and the three numbers correspond to the desired values for the virtual origins for $u$, $w$ and $v$, respectively, i.e. $\ell_u^+$, $\ell_w^+$ and $\ell_v^+$. For the first letter, $F(ull)$ means that the full conditions from Eq. (4) are used, whereas $D(iagonal)$ means that only the three dominant terms, $\mathcal{C}_{uu}$, $\mathcal{C}_{ww}$ and $\mathcal{C}_{vp}$ are used, and the velocities are then uncoupled. The second letter denotes the type of boundary condition used for $u$ and $w$: $H(omogeneous)$ when homogeneous slip lengths are considered, and $I(nhomogeneous)$ when wavelength-dependent coefficients, resulting from the analytical solution of the Stokes equation, are considered. The last letter denotes the type of boundary condition used for $v$: $P$ when an impedance between $v$ and $p$ is imposed (Stokes model), and $v$ when $v = \ell_y dv/dy$ is used instead.

## 4. Results and discussion

From the three virtual origins under study, i.e. $\ell^+ = 1, 2$ and 4, the first two exhibit proportionately the same behaviour, and hence only results for $\ell^+ = 2$ and 4 are presented here. Throughout this section, results are scaled with magnitudes measured at the virtual origin of the mean flow, $\tilde{\delta} = \delta + \ell_U$, so that $\tilde{\delta}$, the half-channel height perceived by the mean flow, is greater than for the smooth case, and $u_\tau = u_{\tau_{y=0}}(\tilde{\delta}/\delta)^{1/2}$. This is essentially equivalent to ascribing the position of a reference smooth wall for comparison where the mean flow perceives it, i.e. at $y^+ = -\ell_U^+$.

We find the different virtual origins by measuring the wall-normal displacement of the mean flow and rms velocity profiles relative to smooth wall data, as was illustrated in Figure 5. The different virtual origins for each case, i.e. $\ell_U^+$, $\ell_u^+$, $\ell_w^+$, $\ell_v^+$, and $\ell_{\omega_x}^+$, are assembled in Table 3. To assess the validity of the off-wall conditions, in Figures 7-13 the profiles are shifted by their

corresponding virtual origins. The degree of resemblance of the shifted profiles to the smooth wall data allows us to determine the degree of success of the technique.

*4.1. Fully coupled boundary conditions*

We first impose the full boundary conditions provided by Eq. (4), with the aim of modelling a smooth wall at $y^+ = -2$ and at $y^+ = -4$. The mean flow and rms fluctuations are portrayed in Figure 7. At a first glance, we can already conclude that case $FP444$ fails to mimic a wall at $y^+ = -4$, while case $FP222$ seems to succeed, as all the shifted curves fall on top of the smooth channel data.

For $FP222$ the mean velocity profile in Figure 7a shows a virtual origin of $\ell_U^+ \approx 2$. Similarly, all the three velocity fluctuations as well as the streamwise vorticity have been shifted towards the wall by 2 wall units with respect to the smooth wall, thereby implying that the virtual origin of the quasi-streamwise vortices is $\ell_{\omega_x}^+ \approx 2$, same as the mean flow. Thus, the boundary conditions have successfully reproduced the effect of having a virtual origin at $y^+ = -2$. The validity of the model for case $FP222$ is confirmed by the spectral density distributions in Figures 8a-c, which show that the distribution of the velocity fluctuations among different length scales agrees reasonably well with that of the smooth channel case. In these figures, the data for case $FP222$ is compared to the corresponding data for a smooth wall at $y_{smooth}^+ = y^+ + \ell^+$.

While the mean profile for $FP222$ collapses with the profile for the corresponding smooth channel, that for $FP444$ exhibits a downward shift of the logarithmic region. This suggests that the model does not merely shift the velocities by the virtual origin, as observed in the rms velocity and $\omega_x^+$ fluctuations shown in Figures 7b-c. For case $FP444$ the near-wall turbulence is completely disrupted compared to a smooth wall case. The peak of the streamwise fluctuations in Figure 7 decays, while that of the streamwise vorticity increases, suggesting a weakening of the streaks and a strengthening of the vortices. Inspecting the spectral energy distributions of the three velocities, Figures 8d-f, the wall-normal velocity exhibits the most dramatic change. The spectrum shows the appearance of new energetic structures, short in $x$ and wide in $z$. The source of the energy can be attributed to the large values of the impedance coefficient $\mathcal{C}_{vp}^+$ assigned to small length scales, as observed in Figure 6a. This will be further discussed in the following subsections.

These results suggest that the conditions derived from considering a Stokes flow underneath are a good model for $\ell^+ \lesssim 2$, but are not valid for $\ell^+ = 4$.

*4.2. Uncoupled boundary conditions*

The implementation of the full conditions from Eq. (4) involves the full coupling between the three velocities and the pressure, which makes setting different virtual origins for each component difficult. In what follows we neglect certain terms while still maintaining a common virtual origin, aiming to decouple the three velocity conditions to later impose different origins. For that, two different approaches are tested: case $DIP222$, where only the dominant term for each velocity component has been retained, i.e. the slip coefficients $\mathcal{C}_{uu}^+$ and $\mathcal{C}_{ww}^+$ for $u$ and $w$, and the transpiration coefficient $\mathcal{C}_{vp}^+$ for $v$; and case $DHP222$ and $DHP444$, similar to the previous case but where homogeneous slip lengths in $x$ and $z$ have been used, removing any dependencies of the slip coefficients on the length scales. The latter is supported by previous studies on slip lengths [14, 13], where they considered homogeneous slip lengths for $u$ and $w$ defined by Robin conditions.

For the case of a virtual origin at $y^+ = -2$, similar results are obtained with the two approaches, $DIP222$ and $DHP222$, as shown in red in Figures 9a-c and 9d-f, respectively. This agrees well with the observations in Section 3.1, where we concluded that $\mathcal{C}_{ww}^+$ and $\mathcal{C}_{uu}^+$ are essentially homogeneous for the energetically significant flow length scales. When comparing the current two cases with the previous case with full off-wall conditions, $FP222$, little difference is

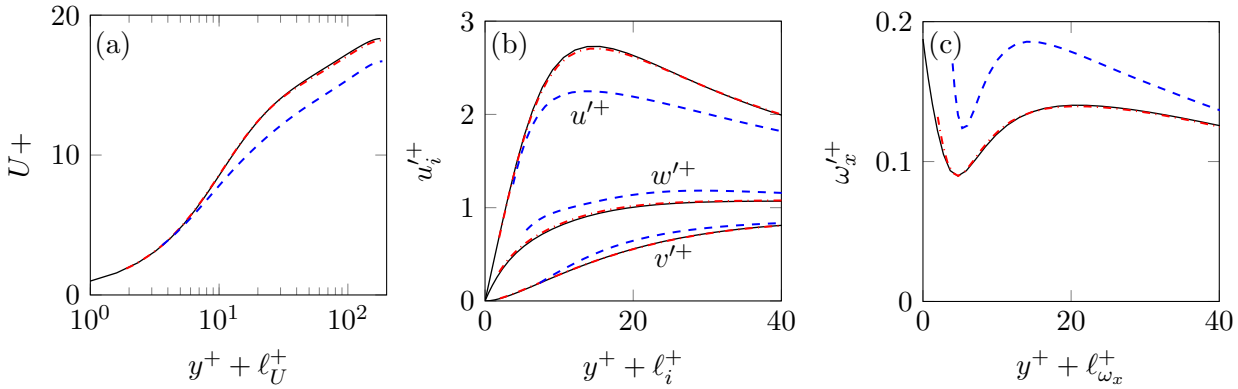


Figure 7: (a) Mean velocity profile shifted by the virtual origin of the mean flow, $\ell_U^+$; (b) rms velocity fluctuations shifted by their corresponding virtual origins, $\ell_u^+$, $\ell_v^+$ and $\ell_w^+$; (c) streamwise vorticity fluctuations shifted by the virtual origin of the vortices. In the case $FP444$ it is shifted by $\ell^+ = 4$. Solid lines, smooth channel; dash-dotted, $FP222$; and dashed, $FP444$.

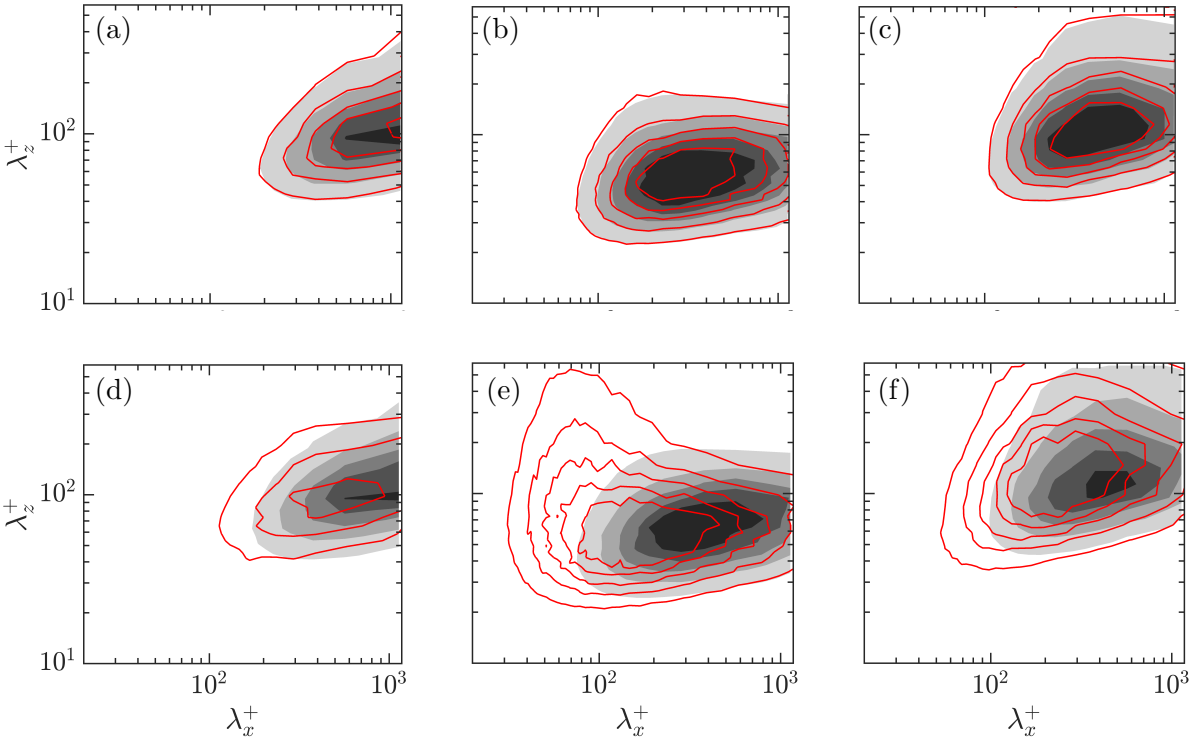


Figure 8: Premultiplied spectral energy densities of the velocity components. (a-c) Case $FP222$. Shaded contours represent the smooth channel at $y^+ \approx 7$ and the solid lines the present DNSs shifted by their corresponding virtual origin, at $y^+ \approx 7 - \ell_i^+$, $\ell_i^+$ being $\ell_u^+$, $\ell_v^+$ and $\ell_w^+$. (a) $k_x k_z E_{uu}$, (b) $k_x k_z E_{vv}$ and (c) $k_x k_z E_{ww}$. (d-f) Case $FP444$. Shaded contours represent the smooth channel at $y^+ \approx 13$ and the solid lines the present DNSs shifted by their corresponding virtual origin. (d) $k_x k_z E_{uu}$, (e) $k_x k_z E_{vv}$ and (f) $k_x k_z E_{ww}$.

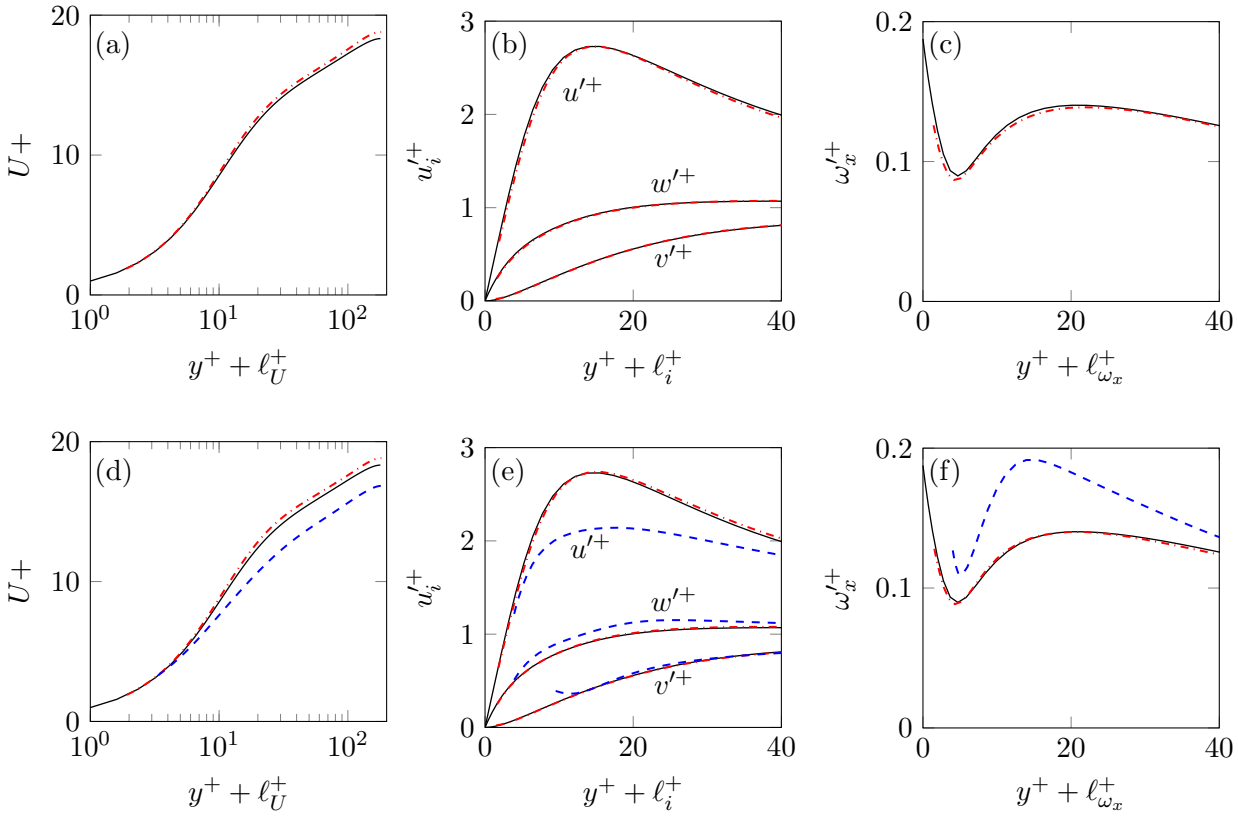


Figure 9: (a,d) Mean velocity profile; (b,e) rms velocity fluctuations where $\ell_i^+ = \ell_u^+$, $\ell_v^+$ and $\ell_w^+$; (c,f) streamwise vorticity fluctuations. (a-c) Solid lines, smooth channel; dash-dotted, case $DIP222$. (d-f) Solid, smooth channel; dash-dotted, case $DHP222$; dashed, case $DHP444$. All results are shifted by their corresponding virtual origins, except for case $DHP444$ in (f), for which the shift is $\ell^+ = 4$.

observed. The mean flows have virtual origins of 2 wall units, same as for $FP222$. The velocity fluctuations, however, are slightly shifted from the $FP222$ case, although it is indiscernible in the figures. In particular, the virtual origin of the wall-normal velocity is slightly less than 2 wall-units, $\ell_v^+ \approx 1.5$. The virtual origin of $\omega_x'$, which relates to the displacement of quasi-streamwise vortices, is also $\ell_{\omega_x}^+ \approx 1.5$, same as $\ell_v^+$. The difference in virtual origins for the mean velocity, $\ell_U^+ \approx 2$, and the streamwise vortices, $\ell_{\omega_x}^+ \approx 1.5$, results in a small upward shift of the log law, as observed in Figure 9a.

For a virtual origin at $y^+ = -4$, only the second approach ($DHP444$) has been tested, obtaining similar results to case $FP444$. This approach failed to model a virtual origin at $y^+ = -4$, as we could expect from the previous case. The $v'^+$ profile in this case diverges even more than before. Although not shown here, in this case the new energetic region observed in the v-spectrum of $FP444$ (see Figure 8e) intensifies, indicating that the disparity between the current case and the corresponding smooth channel is indeed due to the large permeability values at small length scales. In order to eliminate the appearance of the new structures observed in this case, brute-force filtering was also tested in a separate simulation. The boundary condition $v^+ = \mathcal{C}_{vp}^+ p^+$ was applied to large structures only, while structures smaller than $\lambda_x^+ < 50$ and $\lambda_z^+ < 10$ were free to permeate, $dv^+/dy = 0$. However, this was not sufficient to impede the amplification of small length scales. A model that accounts for advective effects in the modelled

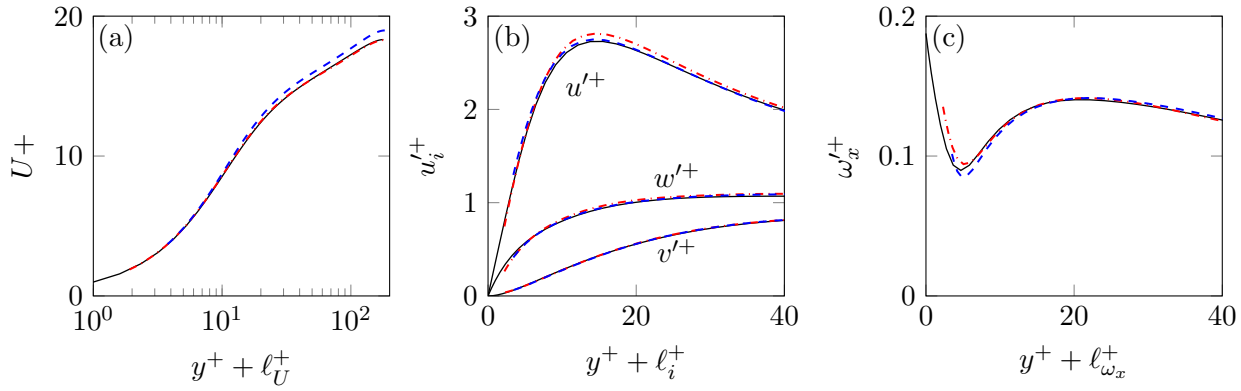


Figure 10: (a) Mean velocity profile; (b) rms velocity fluctuations; (c) streamwise vorticity fluctuations. Solid lines, smooth channel; dash-dotted, $DHV222$; dashed, $DHV444$. All results have been shifted by their corresponding virtual origins.

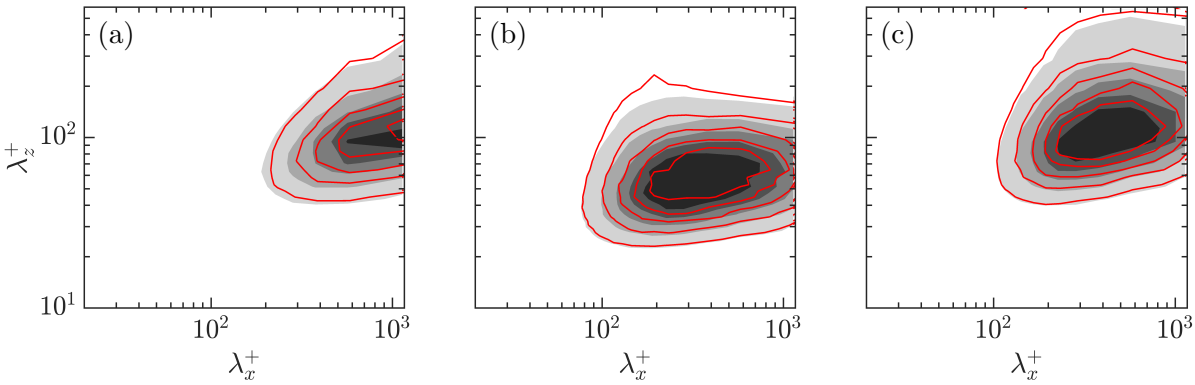


Figure 11: Premultiplied spectral energy densities of the velocity components for $DHV444$. Shaded contours represent the smooth channel at $y^+ \approx 7$ and the solid lines the present DNSs shifted by their corresponding virtual origin, at $y^+ \approx 7 - \ell_i^+$, $\ell_i^+$ being $\ell_u^+$, $\ell_v^+$ and $\ell_w^+$. (a) $k_x k_z E_{uu}$, (b) $k_x k_z E_{vv}$ and (c) $k_x k_z E_{ww}$.

layer may be more suitable for deep virtual origins, but this has been left for future work.

*4.3. Robin conditions for the three velocities*

Since the model constructed from the Stokes equation breaks down for a virtual origin of 4 wall units, a different strategy has been pursued. By analogy with the slip-length model for the tangential velocities, we propose Robin conditions for the three velocities, so that the velocities $u^+$, $v^+$ and $w^+$ are related to their wall-normal gradients by three slip lengths, as in Eq. 3. However, in the wall-normal direction $\ell_y^+$ does not correspond to the virtual origin of $v$. The wall-normal velocity profile is not linear near the wall, unlike the tangential velocities, so the slip length $\ell_y^+$ should differ from the virtual origin $\ell_v^+$ which we intend to model. We set $\ell_y^+$ based on the offset with $\ell_v^+$ observed for smooth walls, as previously indicated in Figure 5b, that is, $\ell_y^+ = \ell_v^+ - \ell_{sm}^+$.

Comparing to the previous model, this technique produces a significant improvement on the results, as shown in Figures 10 and 11. This model reproduces with reasonable accuracy not only a virtual origin at $y^+ = -2$, but also that at $y^+ = -4$. For the latter, the displacements of the

$v'^+$ and $w'^+$ profiles are not exactly 4 wall units, but $\ell_v^+ \approx 3.5$ and $\ell_w^+ \approx 3.0$. The virtual origin for the quasi-streamwise vortices is also $\ell_{\omega_x}^+ \approx 3.0$, as observed in Figure 10c, which coincides with $\ell_w^+$. This agreement between the origin for the vortices and that for the spanwise velocity may be attributed to $\ell_w^+$ being the most restrictive origin between those of $v$ and $w$. Since in this case the virtual origin of $w$ is the shallowest of all the three velocities, i.e. $\ell_w^+ < \ell_v^+ < \ell_u^+$, the displacement of quasi-streamwise vortices would be limited by $w$, which would explain why $\ell_{\omega_x}^+ = \ell_w^+$. However, the virtual origins in this case are too close for the evidence to be conclusive. The relation between virtual origins will be analysed in the next section. The small difference between the virtual origin for the mean and that for the vortices translates into a slight shift upwards of the mean profile with respect to the smooth channel.

From these results, we can conclude that the Robin boundary conditions reproduce successfully, and in a simple manner, the effect of a virtual origin. Case $DHV444$ could be further improved by imposing a slightly larger $\ell_z^+$ than 4 wall units, since at 4 wall units the spanwise velocity profile is no longer linear, and $\ell_w^+$ differs from $\ell_z^+$. More accurate results would be obtained if the spanwise slip-length was defined similarly to how $\ell_y^+$ was calculated in this section, so that the origin of the spanwise velocity would lie at $y^+ = -4$.

*4.4. Different virtual origins for the tangential velocities and for v*

In this section, we impose a different origin for $v$ than those for $u$ and $w$. Two cases will be presented, case $DHV220$ and $DHV440$ with $\ell_x^+ = \ell_z^+ = 2$ and 4, respectively, while keeping the impermeability condition at the simulation boundary, i.e. $\ell_y^+ = 0$, similar to [13].

For cases $DHV220$ and $DHV440$, the virtual origins for the mean flow are $\ell_U^+ \approx 2$ and 4, respectively, as shown in Figure 12a. However, the mean velocity profiles experience an upward shift of the logarithmic region relative to the smooth case, which directly relates to a reduction of drag. As imposed by $\ell_x^+$ and $\ell_z^+$, $u'^+$ and $w'^+$ profiles go to zero at $y^+ \approx -2$ and $y^+ \approx -4$ when linearly extrapolated, which correspond approximately to the virtual origins. The wall-normal velocity profiles are also shifted relative to the smooth profile, meaning that the virtual origin of $v$ is not zero. Although $v = 0$ at the wall, i.e. $\ell_y^+ = 0$, its slope $dv/dy$ is no longer zero due to continuity. Thus the vertical displacement of the $v'^+$ profile results in a non-zero virtual origin for $v$, $\ell_v^+ \approx 1.3$ for case $DHV220$ and $\ell_v^+ \approx 1.7$ for $DHV440$.

The resulting virtual origins for the quasi-streamwise vortices are $\ell_{\omega_x}^+ \approx 1.3$ for case $DHV220$ and $\ell_{\omega_x}^+ \approx 1.7$ for $DHV440$, which coincide with the corresponding virtual origins for $v$. The reason is that in these cases the downward displacement of the vortices is restricted by $v$ being zero at the simulation boundary, as discussed in Section 2. The vortices approach the wall, as they are allowed to slip in the spanwise direction, and their approach corresponds with the origin perceived by the wall-normal velocity, which is the shallowest origin between $\ell_v^+$ and $\ell_w^+$. Hence, the virtual origin for the vortices in these cases appears to be determined by the origin for the wall-normal velocity.

The fact that the origin for the mean flow is deeper than that for the vortices translates into a reduction of skin friction, as observed in the upward shift of the mean velocity profile in the log law region. Hence, a $\Delta U^+ > 0$ is obtained despite the slip lengths in the streamwise and spanwise directions being equal, due to the wall-normal velocity having a shallower virtual origin. Furthermore, as discussed in Section 2, in these cases the change $\Delta U^+$ should be well defined by $\Delta U^+ \propto \left(\ell_x^+ - \ell_{z,eff}^+\right)$. This is indeed the case. The values of $\ell_{\omega_x}^+$ agree reasonably well with the empirical function for the effective spanwise slip length in Eq. (2), which gives $\ell_{z,eff}^+ = 1.3$ and 2.0. Therefore, $\ell_{z,eff}^+$ can be interpreted as an expression to predict $\ell_v^+$, and equivalently $\ell_{\omega_x}^+$, when $\ell_y^+ = 0$. These results support the idea that the change in drag is due to the displacement of the mean flow with respect of the quasi-streamwise vortices, and clarify the saturation effect of the spanwise slip length observed for large $\ell_z^+$.

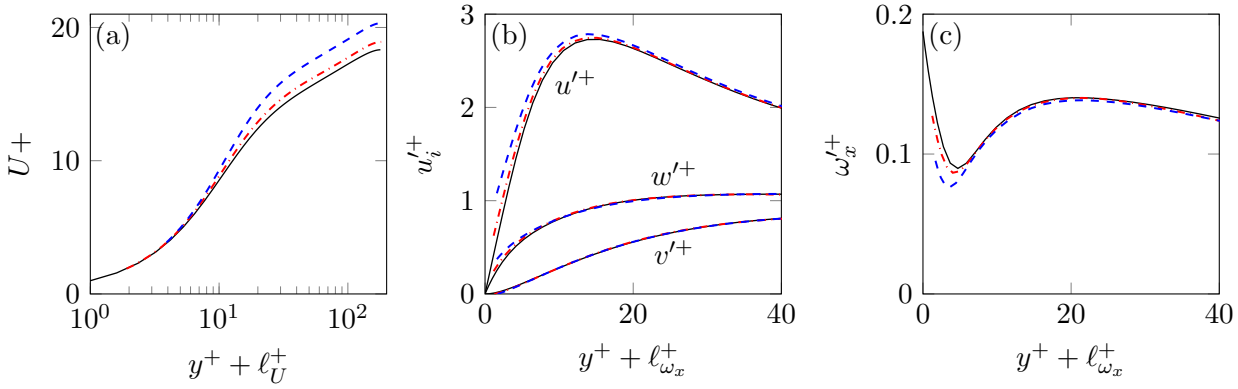


Figure 12: (a) Mean velocity profile shifted by the virtual origin of the mean flow, $\ell_U^+$; (b) rms velocity fluctuations shifted by the virtual origin of the vortices, $\ell_{\omega_x}^+$; (c) streamwise vorticity fluctuations shifted by $\ell_{\omega_x}^+$. Solid, smooth channel; dash-dotted, $DHV220$; dashed, $DHV440$.

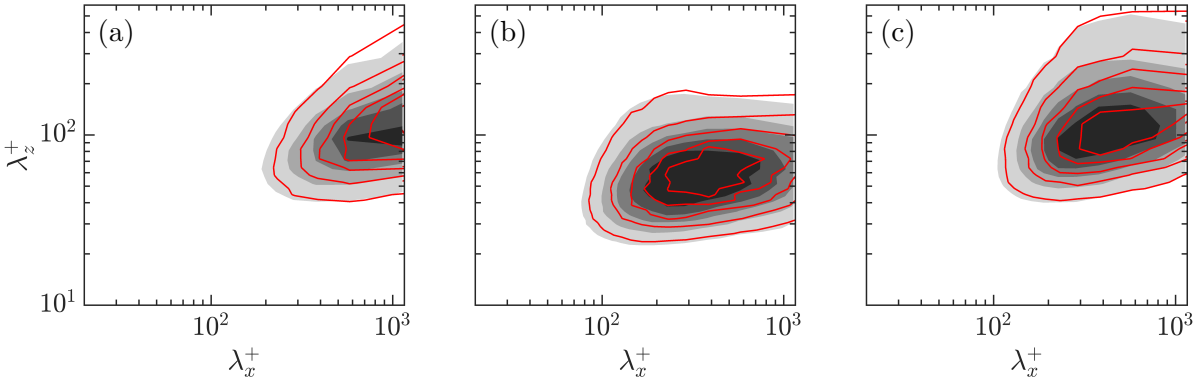


Figure 13: Premultiplied spectral energy densities of the velocity components for $DHV440$. Shaded contours represent the smooth channel at $y^+ \approx 7$ and the solid lines the present DNSs shifted by the virtual origin of the vortices, at $y^+ \approx 7 - \ell_{\omega_x}^+ = 5.3$. (a) $k_x k_z E_{uu}$, (b) $k_x k_z E_{vv}$ and (c) $k_x k_z E_{ww}$.

In Figure 12b, all the three velocity rms's have been shifted by the virtual origin of the vortices, achieving a better match with the smooth channel data than when shifting by their corresponding virtual origins. This implies that the origin of all three velocity rms's is represented well by the virtual origin of the vortices, even if the streamwise and spanwise profiles have a different slope at $y^+ = 0$, enforced by the boundary conditions implemented. The slip-lengths modify the origin of the near-wall turbulence and the near-wall cycle is shifted in block by $\ell_{\omega_x}^+$. This is confirmed by the good agreement of the spectral energy distributions observed in Figure 13 for $DHV440$, where the spectra of the present case are superimposed over the smooth channel data displaced by the virtual origin of the vortices, i.e. at $y^+ + \ell_{\omega_x}^+$.

## 5. Generalisation of the linear slip-length model

In this section we review the linear theory of slip lengths [6, 7]. From the present results, we confirm the existing understanding that the change in friction is caused by the difference between the virtual origins for the mean flow and that for quasi-streamwise vortices. However, the origin for the vortices is not completely defined by $\ell_z^+$ alone, as originally postulated in [5, 7]. We

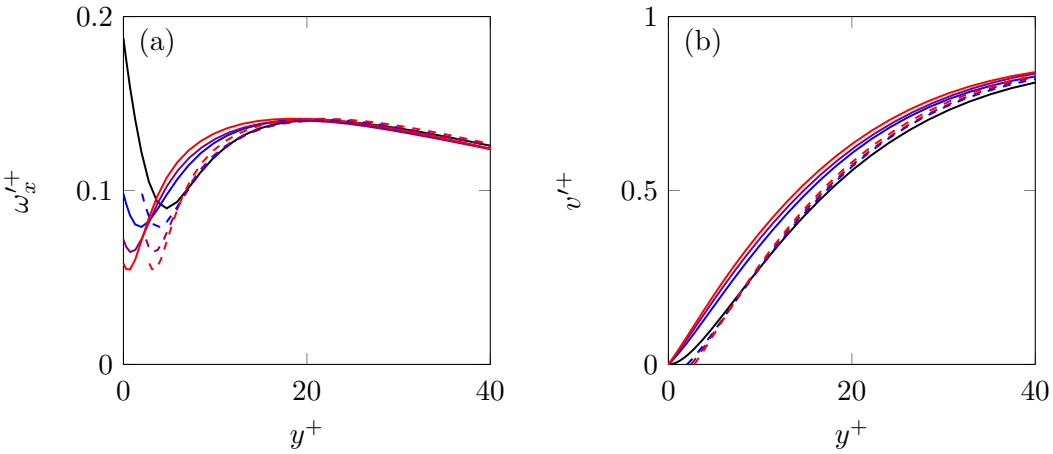


Figure 14: Rms fluctuations of (a) the streamwise vorticity and (b) the wall-normal velocity, for simulations with $\ell_x^+ = \ell_z^+$ and $\ell_y^+ = 0$. Black curves represent the smooth wall case for reference. Blue, $\ell_x^+ = \ell_z^+ = 4.2$; purple, $\ell_x^+ = \ell_z^+ = 6.7$; red, $\ell_x^+ = \ell_z^+ = 10$. The dashed lines correspond to the solid lines shifted by $\ell_{z,eff}^+$, as defined in Eq.2. Data from [24].

propose to generalise the existing linear theory to

$$\Delta U^+ \propto \left(\ell_U^+ - \ell_{\omega_x}^+\right). \tag{5}$$

We can expect $\ell_U^+ \approx \ell_x^+$, since in the viscous sublayer the mean velocity profile is essentially linear, and both $\ell_U^+$ and $\ell_x^+$ can be used interchangeably. However, contrary to the linear theory of slip lengths, the origin of the vortices is not given by the spanwise slip length alone, but by a combination of the spanwise and wall-normal slip lengths, $\ell_z^+$ and $\ell_y^+$. We suggest that $\ell_{\omega_x}^+$ is determined by the most restrictive virtual origin between that of $v$ and $w$, that is, by the shallowest between $\ell_w^+$ and $\ell_v^+$. Although $\ell_w^+$ and $\ell_v^+$ are only known a posteriori, we could predict $\ell_{\omega_x}^+$ from the slip-lengths $\ell_y^+$ and $\ell_z^+$. It has been empirically found that when the wall-normal velocity is set to zero at the simulation boundary (i.e. $\ell_y^+ = 0$), $\ell_{\omega_x}^+$ can be approximated by the expression in Eq. 2, as shown in Figure 2b.

To further support this idea, Figure 14 shows results for additional simulations with larger $\ell_x^+ = \ell_z^+$ and $\ell_y^+ = 0$ from [24]. The values of the slip lengths are chosen beyond the linear regime, where the saturation effect of the spanwise slip is clearly observed. As shown in Figure 14a, the vortices approach the wall as the slip lengths increase. Their displacement or virtual origin is captured here by $\ell_{z,eff}^+$ (Eq. 2), since when displaced by $\ell_{z,eff}^+$, the curves collapse with the smooth channel data. The profiles of $v'^+$ in Figure 14b also experience the same displacement, i.e. $\ell_v^+ \approx \ell_{\omega_x}^+ \approx \ell_{z,eff}^+$, as the displacement of the vortices is limited by $v$ being zero at the simulation boundary.

The expression in Eq. 2 could still be expanded for $\ell_y^+ \neq 0$, at least when $\ell_y^+ < \ell_z^+$. Assuming that only the difference between the origins for the different velocities can have an effect, the problem has only two degrees of freedom. A change of frame of reference to $y^+ = -\ell_y^+$ shows that the same result would be obtained for slip lengths 0 in $y$, $\ell_x^+ - \ell_y^+$ in $x$ and $\ell_z^+ - \ell_y^+$ in $z$. The resulting change in drag should then be given by

$$\Delta U^+ \propto \left(\ell_x^+ - \ell_y^+\right) - \frac{\left(\ell_z^+ - \ell_y^+\right)}{1 + \left(\ell_z^+ - \ell_y^+\right)/4}. \tag{6}$$

However, in order to generalise for any $\ell_z^+$ and $\ell_y^+$, cases with $\ell_v^+ > \ell_w^+$ should also be studied in the future. The distance of the quasi-streamwise vortices to the wall is essentially governed by

the ability of the induced cross-flow to approach the surface. We would therefore expect $\ell^+_{\omega_x}$ to depend only on $\ell^+_y$ and $\ell^+_z$. The *w-control* case from Choi *et al.* [18] provides some insight into this dependence when $\ell^+_v > \ell^+_w$. The drag reduction obtained with *w-control*, where $\ell^+_w \approx 0$ but $\ell^+_v$ is finite, was practically equal to that obtained with *v-w-control*, where both $\ell^+_v \approx \ell^+_w \approx 0$. This would suggest that with *w-control* the origin of the vortices is essentially the same as with *v-w-control*, that is, that in both cases $\ell^+_{\omega_x} \approx 0$. Therefore when $\ell^+_v > \ell^+_w$, it appears that the origin for the vortices is governed by that of the spanwise velocity, where $\ell^+_{\omega_x} \approx \ell^+_w \approx \ell^+_z$. This observation is however preliminary, and needs to be further investigated.

## 6. Conclusions

Complex surfaces can reduce drag if they induce a greater resistance to the induced, secondary cross-flow than to the mean, streamwise flow. Previous studies by Luchini *et al.* [6] and Jiménez [7] proposed that the drag reduction produced by these surfaces could be quantified by the difference between the virtual origins, measured from a reference 'wall' plane, of the mean velocity and of the spanwise flow induced by the quasi-streamwise vortices. This was expressed as the difference between the streamwise and spanwise slip lengths, $\ell^+_x - \ell^+_z$. The slip-length model, however, neglects the effect of non-zero wall-normal velocity at the reference plane, which can be significant for the drag. In terms of the virtual origin for the vortices, and for slip lengths greater than a few wall units, the wall-normal velocity induced is no longer negligible and the virtual origin of $v$ also needs to be considered. Otherwise, a saturation of the effect of the spanwise slip is observed [13]. In this paper, a distinction has been made between slip lengths and virtual origins. The slip lengths $\ell^+_x$, $\ell^+_z$ and $\ell^+_y$ are defined as the constants of proportionality between the respective velocity components and their wall-normal gradients, and the virtual origins $\ell^+_u$, $\ell^+_w$ and $\ell^+_v$ as the origins effectively perceived by the three velocity components.

In the present work we have explored two methods to represent virtual origins below the plane where boundary conditions are imposed, through a Stokes model for the flow beneath, and through Robin conditions for the three velocity components. We restrict ourselves to virtual origins of a few wall units, which modulate the near-wall turbulent cycle without completely destroying it. The models would therefore not be applicable, for instance, to fully rough surfaces. We first developed the models in the framework of equal virtual origins, that is, to model the presence of an underlying smooth wall. The first model gave satisfactory results for a virtual origin of up to 2 wall units, but failed for a virtual origin of 4 wall units. This was caused by the large effective permeability at small length scales, which excited short and wide, artificial structures in the flow. The second method, on the other hand, proved to hold at least up to a virtual origin 4 wall units below the simulation boundary, although further refinement is currently under investigation.

The latter model was then applied on simulations with different virtual origins for the different velocity components. We have conducted DNSs with equal slip lengths in the tangential directions, $\ell^+_x = \ell^+_z$, while keeping $v = 0$ at the simulation boundary, i.e. $\ell^+_y = 0$. The results are consistent with the change in drag being due to the difference between the virtual origins for the mean flow and for quasi-streamwise vortices. The origin for the mean flow is essentially determined by $\ell^+_x$, while the origin for the vortices is given by a combination of the spanwise and wall-normal slip lengths, i.e. $\ell^+_z$ and $\ell^+_y$. The results suggest that the origin of the vortices, $\ell^+_{\omega_x}$, is mainly determined by the smallest origin between $\ell^+_w$ and $\ell^+_v$, which is the one that restricts more intensely the cross flow induced by the vortices. Accounting for a non-zero $\ell^+_v$ and its effect on $\ell^+_{\omega_x}$ allows us to generalise the slip-length theory of Luchini *et al.* [6] and Jiménez [7]. When $\ell^+_y = 0$, we observe that a good approximation for $\ell^+_{\omega_x}$ is $\ell^+_{\omega_x} \approx \ell^+_v \approx \ell^+_z/(1 + \ell^+_z/4)$. The simulations of [18] suggest that $\ell^+_v < \ell^+_w$ results in $\ell^+_{\omega_x} \approx \ell^+_w \approx \ell^+_z$, but additional simulations need to be conducted to find a general expression for $\ell^+_{\omega_x}$. Further research also needs to be

conducted to extend the models to surfaces which select certain modes at the interface, such as superhydrophobic posts [17] or deep transverse grooves [25].

**Acknowledgements**
This work was partially supported by the Coturb program of the European Research Council. GG was supported by an educational grant from Fundación Bancaria 'la Caixa'. CTF was supported by Engineering and Physical Sciences Research Council. The authors are grateful to C. Sanmiguel for insightful refereeing comments.

**References**

[1] R. García-Mayoral and J. Jiménez. Hydrodynamic stability and breakdown of the viscous regime over riblets. *J. Fluid Mech.*, 678:317–347, 2011.
[2] J. P. Rothstein. Slip on superhydrophobic surfaces. *Annu. Rev. Fluid Mech.*, 42:89–109, 2010.
[3] S. Hahn, J. Je, and H. Choi. Direct numerical simulation of turbulent channel flow with permeable walls. *J. Fluid Mech.*, 450:259–285, 2002.
[4] N. Abderrahaman-Elena and R. García-Mayoral. Analysis of anisotropically permeable surfaces for turbulent drag reduction. *Phys. Rev. Fluids*, 2:114609, 2017.
[5] P. Luchini, F. Manzo, and A. Pozzi. Resistance of a grooved surface to parallel flow and cross-flow. *J. Fluid Mech.*, 228:87–109, 1991.
[6] P. Luchini. Reducing the turbulent skin friction. *Proc. 3rd ECCOMAS CFD Conf.*, pages 466–470, 1996.
[7] J. Jiménez. On the structure and control of near wall turbulence. *Phys. Fluids*, 6:944, 1994.
[8] F. H. Clauser. The turbulent boundary layer. *Adv. App. Mech.*, 4:1–51, 1956.
[9] D.W. Bechert, M. Bruse, W. Hage, J. G. T. Van der Hoeven, and G. Hoppe. Experiments on drag-reducing surfaces and their optimization with an adjustable geometry. *J. Fluid Mech.*, 338:59–87, 1997.
[10] J. Seo and A. Mani. On the scaling of the slip velocity in turbulent flows over superhydrophobic surfaces. *Phys. Fluids*, 28:025110, 2016.
[11] C. T. Fairhall and R. García-Mayoral. Inhomogeneity of the slip-lengths for simulations over superhydrophobic surfaces. *Flow Turbul. Combust.*, under revision.
[12] K. Fukagata, N. Kasagi, and P. Koumoutsakos. A theoretical prediction of friction drag reduction in turbulent flow by superhydrophobic surfaces. *Phys. Fluids*, 18(5):16–20, 2006.
[13] A. Busse and N. D. Sandham. Influence of an anisotropic slip-length boundary condition on turbulent channel flow. *Phys. Fluids*, 24:055111, 2012.
[14] T. Min and J. Kim. Effects of hydrophobic surface on skin-friction drag. *Phys. Fluids*, 16:L55, 2004.
[15] J. Jiménez, M. Uhlmann, A. Pinelli, and G. Kawahara. Turbulent shear flow over active and passive porous surfaces. *J. Fluid Mech.*, 442:89–117, 2001.
[16] W. P. Breugem and B. J. Boersma. Direct numerical simulations of turbulent flow over a permeable wall using a direct and a continuum approach. *Phys. Fluids*, 17:1–15, 2005.
[17] J Seo, R García-Mayoral, and A Mani. Turbulent flows over superhydrophobic surfaces: flow-induced capillary waves, and robustness of air-water interfaces. *J. Fluid Mech.*, 835:448–473, 2018.
[18] H. Choi, P. Moin, and J. Kim. Active turbulence control for drag reduction in wall-bounded flows. *J. Fluid Mech.*, 262:75–110, 1994.
[19] H. Le and P. Moin. An improvement of fractional step methods for the incompressible Navier-Stokes equations. *J. Comput. Phys.*, 92(2):369–379, 1991.
[20] Y. Mizuno and J. Jiménez. Wall turbulence without walls. *J. Fluid Mech.*, 723:429–455, 2013.
[21] M. P. Encinar, R. García-Mayoral, and J. Jiménez. Scaling of velocity fluctuations in off-wall boundary conditions for turbulent flows. *J. Phys. Conf. Ser.*, 506:012002, 2014.
[22] H. J. Bae, A. Lozano-Durán, S. T. Bose, and P. Moin. Turbulence intensities in large-eddy simulation of wall-bounded flows. *Phys. Rev. Fluids*, 3:014610, 2018.
[23] C. Sanmiguel Vila and O. Flores. Identifying vertical velocity eddies from wall-pressure. *J. Phys. Conf, Ser.*, this volume, 2018.
[24] C. T. Fairhall and R. García-Mayoral. The application of slip length models to larger textures in turbulent flows over superhydrophobic surfaces. *Bull. Am. Phys. Soc.*, 62(14):F13–9, 2017.
[25] M. MacDonald, A. Ooi, R. García-Mayoral, N. Hutchins, and D. Chung. Direct numerical simulation of high aspect ratio spanwise-aligned bars. *J. Fluid Mech.*, under revision.